Supplementary Information (SI) for Green Chemistry.
This journal is © The Royal Society of Chemistry 2026

Supporting Information

Interfacially Engineered MXene Hydrogel with Dual-Conductive Networks for High-Performance Multifunctional Sensing via a Green and Sustainable Strategy

Runfeng Zhang, Yan Zhang, Zongmao Lv, Hai Yu, Jie Liu, Xuejing Zheng, Keyong Tang*

Molecular dynamics simulation

To investigate the dispersion behavior of MXene and the role of PA as a green dispersant, molecular dynamics simulations were performed in this study. Model construction was carried out using Materials Studio 2023 software, calculations were executed with the LAMMPS 2024 package, and trajectory visualization and data analysis were completed in OVITO software. Two three-dimensional systems with periodic boundary conditions were constructed in cubic boxes with dimensions of 8.5 × 8.5 × 8.5 nm^3: System A contained 20,000 water molecules and four MXene nanosheets (labeled 1–4 for identification), while System B additionally included eight PA molecules based on System A to examine the effect of PA on MXene dispersion performance. The size of MXene is 14.192* 17.637* 16.018Å. The initial configurations clearly defined atomic positions and the bonding topology of the MXene structures. Water molecules were described using the TIP3P force field, MXene nanosheets were modeled using the Universal Force Field (UFF), while interactions of other atoms in the system (including PA molecules) were described using the all-atom OPLS force field. Atomic charges were calculated using the restrained electrostatic potential (RESP) method to ensure the accuracy of electrostatic interactions. Short-range van der Waals interactions were described using the Lennard-Jones potential with a cutoff radius of 12 Å, and geometric mixing rules were employed to optimize cross-term parameters; long-range Coulomb interactions were handled using the Particle–Particle Particle–Mesh (PPPM) algorithm with a relative accuracy threshold set to 1×10^{-4} to ensure controlled error in charge distribution calculations. For bonded interactions, chemical bond vibrations and angle bending were described using harmonic potentials, dihedral torsions were treated using a hybrid OPLS/harmonic potential, and improper dihedral configurations were constrained using the cvff potential. Prior to formal simulations, global potential energy surface searching was performed using the conjugate gradient algorithm for energy minimization, with dual convergence criteria for energy and force both set to 1×10^{-15} (in reduced units) and the maximum number of iterations extended to 10^6 to ensure thorough relaxation to local minima. Initial atomic velocities were then generated using the velocity command to create a Maxwell–Boltzmann distribution corresponding to the target temperature. All simulations were conducted in the isothermal–isobaric (NPT) ensemble, with temperature maintained at 298 K using a Nosé–Hoover thermostat (coupling constant 0.1 ps) and pressure

maintained at 101 kPa using a Nosé–Hoover barostat (coupling constant 1.0 ps). A time step of 1 fs was used throughout, with a total simulation time of 1 ns, and trajectory files were output every 1 ps for subsequent analysis. Intermolecular distances and mean square displacement were calculated from LAMMPS trajectories, and spatial clustering analysis was performed using OVITO with a cutoff radius of 4.5 Å consistent with typical hydrogen bonding distances to identify cluster configurations. Representative snapshots were extracted for structural characterization of the dispersion states.

Mechanical testing

Tensile tests were performed on rectangular hydrogel samples (30 mm × 10 mm × 2 mm) at 25 °C using a physical property analyzer (TA.HD Plus, UK) equipped with a 5 kg load cell. The sample was stretched at a constant rate of 2 mm·s^{-1}. The tensile strain (ε) was calculated as the ratio of the elongation (ΔL) to the original gauge length (L_0). The toughness (T), defined as the area under the stress–strain curve up to the point of fracture, was computed according to Equation (S1):

$$T = \int_{\varepsilon_0}^{\varepsilon_f} \sigma(\varepsilon) d\varepsilon \quad \text{(S1)}$$

where, ε_0 and ε_f represent the initial tensile strain and the strain at fracture, respectively.

The self-adhesion strength was tested with a physical property analyzer (TA. HD Plus, UK). Uncontaminated paper, plastic, rubber and glass substrates were cut into rectangular specimens of 40 mm in length and 15 mm in width. A hydrogel sample was sandwiched between two substrates with an area of 10 × 10 mm^2. The sample was subjected to a standard tensile shear test at a speed of 2 mm/min at 25 °C. In addition, cyclic adhesion tests were carried out to evaluate the effect of repeated loading on the adhesion strength of hydrogels.

Conductivity testing: The resistance of the composite hydrogel was measured using a two-probe system (KEYSIGHT 34972A). The bulk resistance (R_b) of the composite hydrogel was recorded, and the conductivity (σ, S m-1) was calculated according to Equation (S2):

$$\sigma = \frac{L}{RbAs} \quad \text{(S2)}$$

where R_b is the bulk resistance, Ω; L is the length of the hydrogel; A_s is the cross-sectional area of the hydrogel, m^2.

Electrical performance and sensing test

The strain sensing performance of the composite hydrogel was evaluated using a resistance meter (KEYSIGHT 34972A) combined with a physical property analyzer Through gauge factor (GF), which characterizes the sensitivity of the hydrogel's sensing performance, was calculated based on its relative resistance change using Equation (S3):

$$GF = \frac{\Delta R/R0}{\varepsilon} = \frac{(R - R0)/R0}{\varepsilon} \quad \text{(S3)}$$

where ε is the applied strain, R_0 is the original resistance value, Ω, and R is the real-time resistance of the hydrogel, Ω.

In addition, the hydrogel-based sensor was attached to various body parts of volunteers—including finger joints, wrists, elbows, knees, and throats—using copper electrodes to enable real-time monitoring of human motion.

Electrophysiological test

The composite hydrogel was fabricated into flexible bioelectrodes of size 20 × 20 mm for recording biopotential signals, specifically electrocardiogram (ECG) and electromyography (EMG). Singal acquisition was performed using a multi-channel physiological acquisition and processing system (RM6240XC, China). During ECG recording, the electrode was placed on the left chest region of the volunteer; for EMG measurement, it was was attached to the volunteer's left forearm. All experiments were conducted with the explicit consent of the participants. It was confirmed that the use of such wearable hydrogel electrodes in this study did not require approval from an institutional review board.

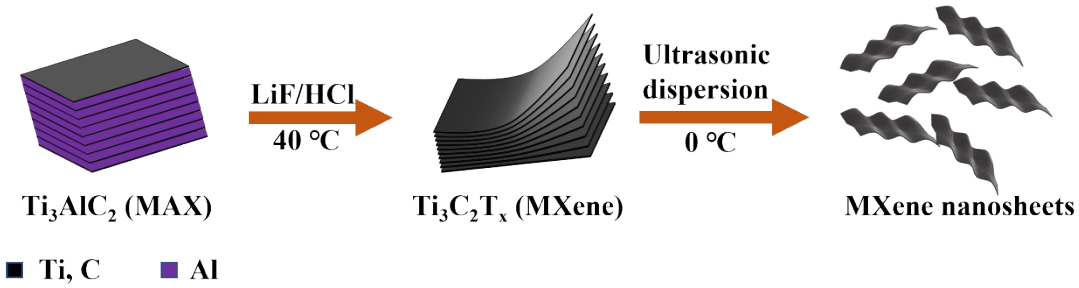

Fig. S1. The schematic diagram of the preparation process of MXene.

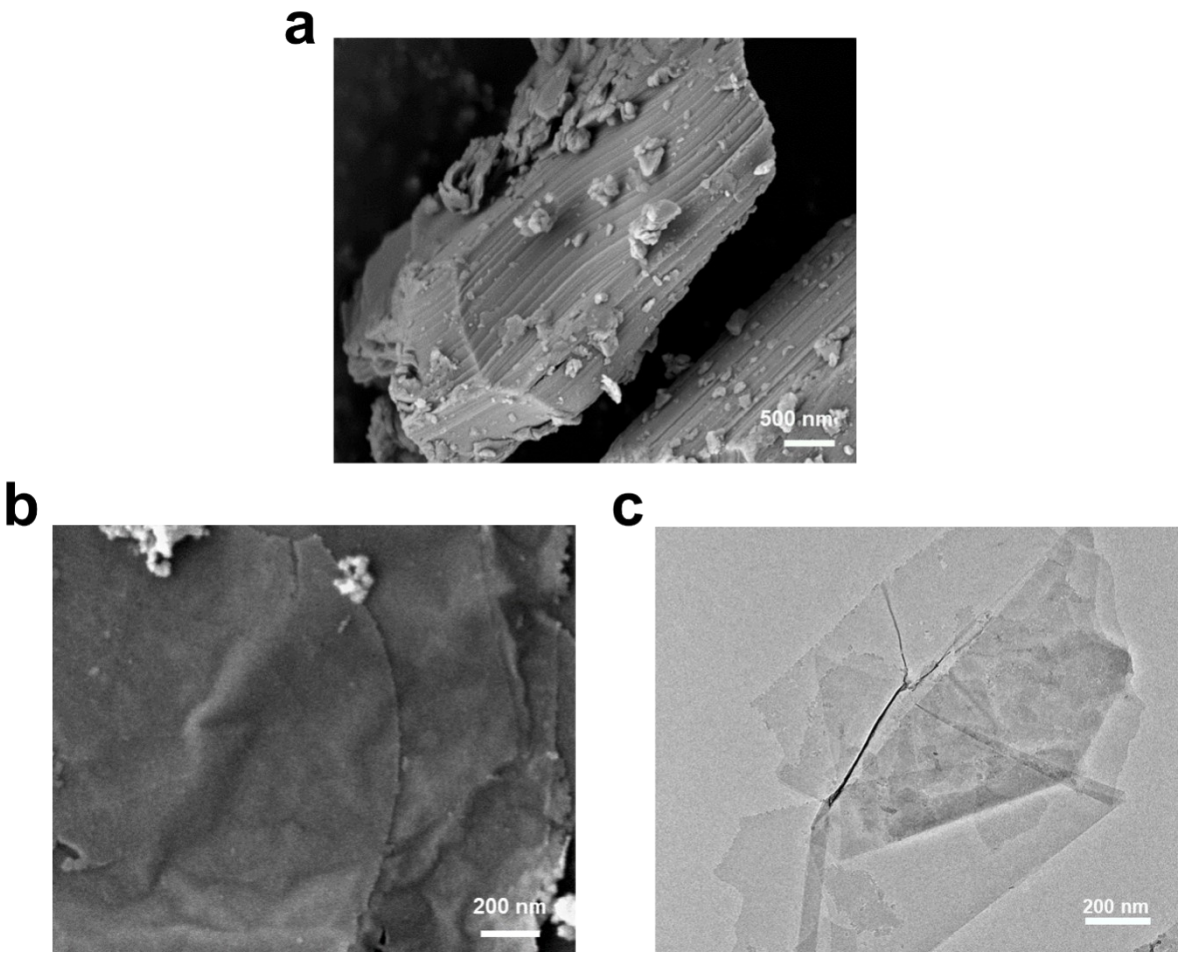

Fig. S2. Morphology of MAX and MXene. (a) SEM image of Ti_3AlC_2 MAX. (b) SEM and (c)TEM images of a few-layer Ti_3C_2 MXene nanosheet.

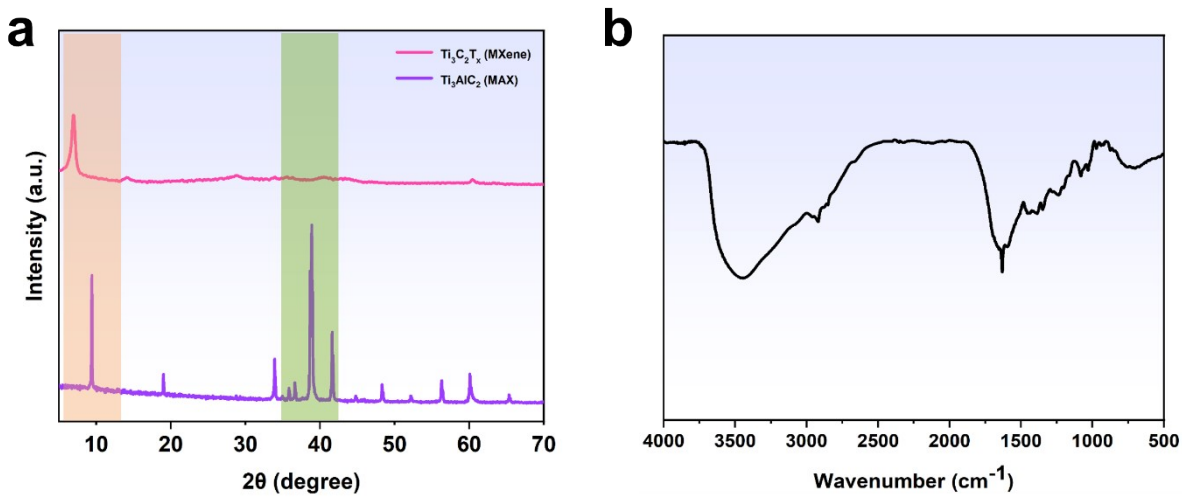

Fig. S3. (a) XRD patterns of MAX and MXene. (b) FT-IR spectrum of MXene.

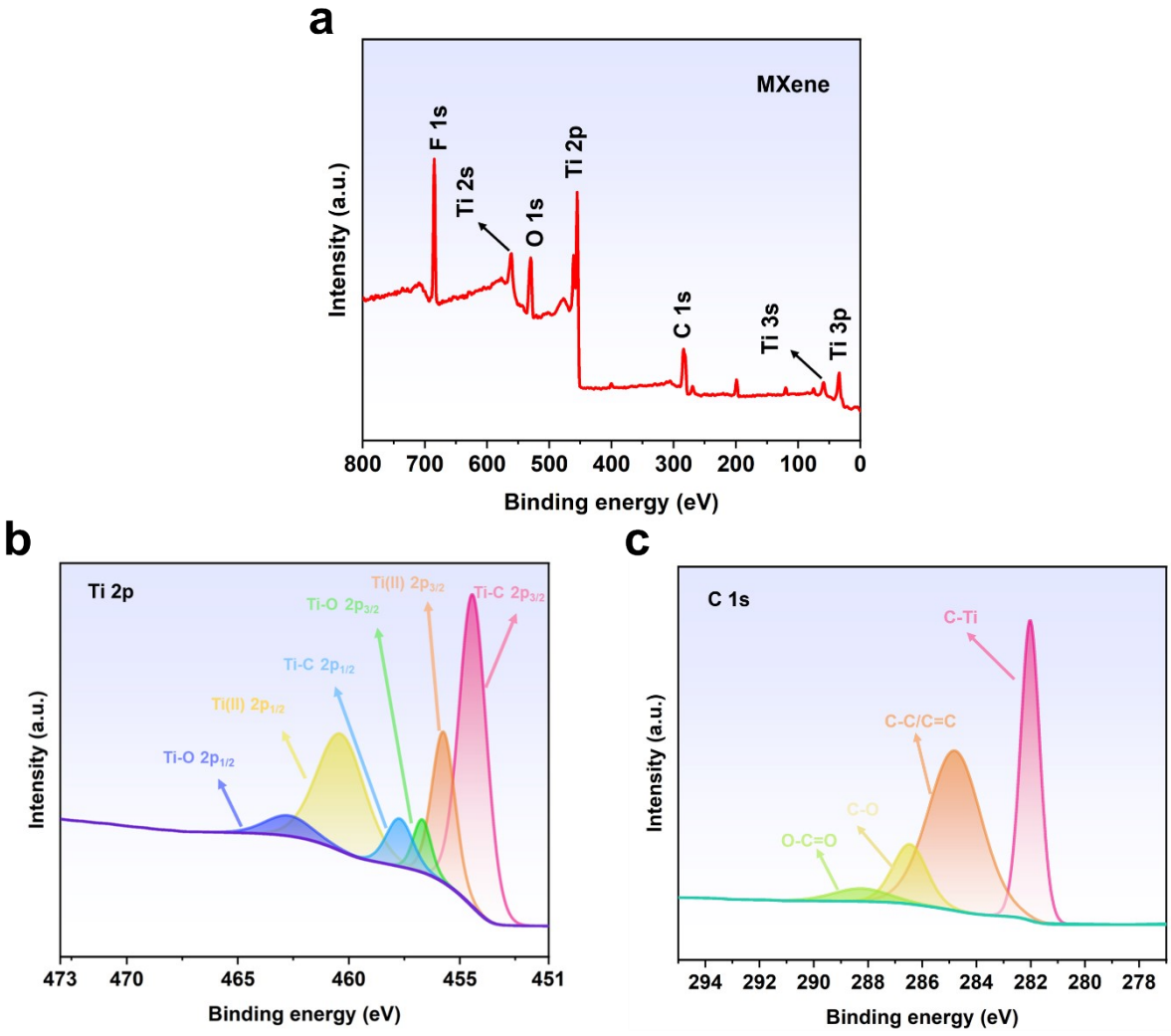

Fig. S4. XPS characterization of the synthesized MXene. (a) Full survey scan spectrum. High-resolution spectra of (b) Ti 2p and (c) C 1s core levels.

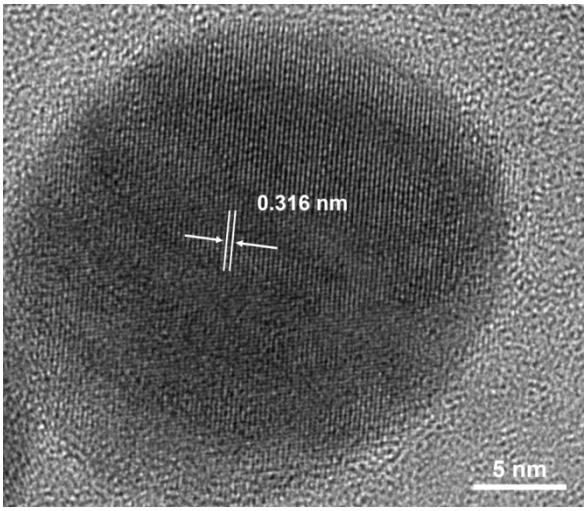

Fig. S5. High-resolution electron microscope image of AgNPs.

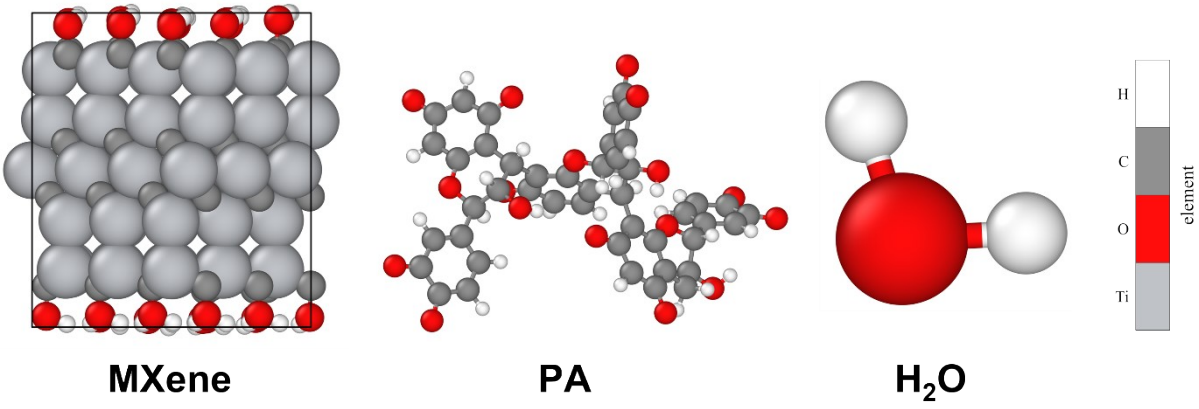

Fig. S6. The structures of MXene, PA and water molecules.

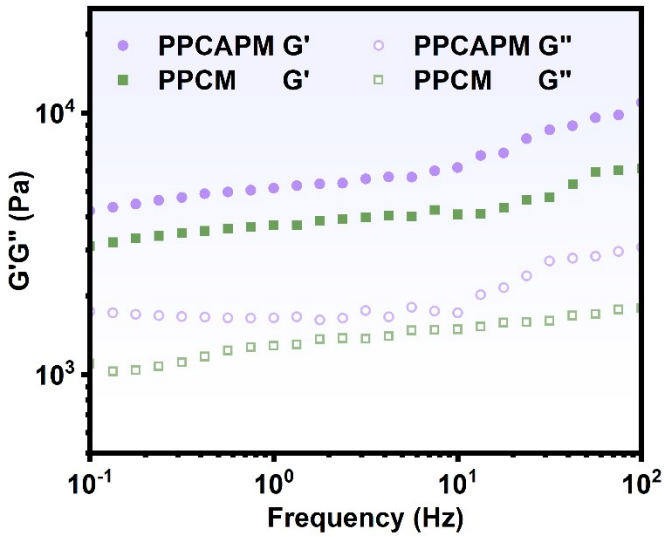

Fig. S7. Dynamic frequency sweep curves of the PPCAPM and PPCM hydrogel..

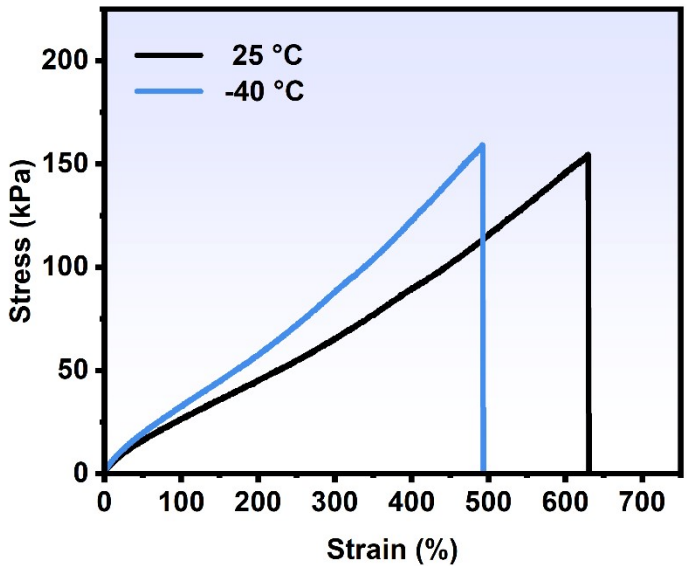

Fig. S8. Changes in mechanical properties of PPGAPM composite hydrogels at -40 ° C.

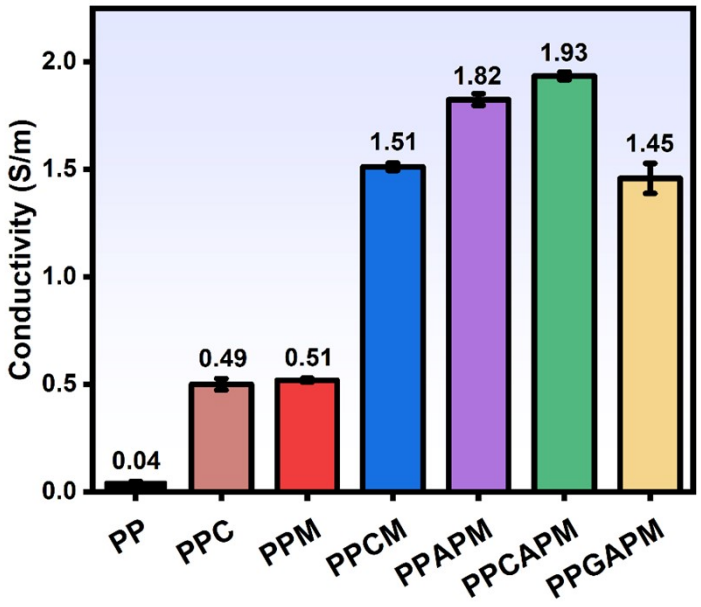

Fig. S9. The electrical conductivity of various composite hydrogels.

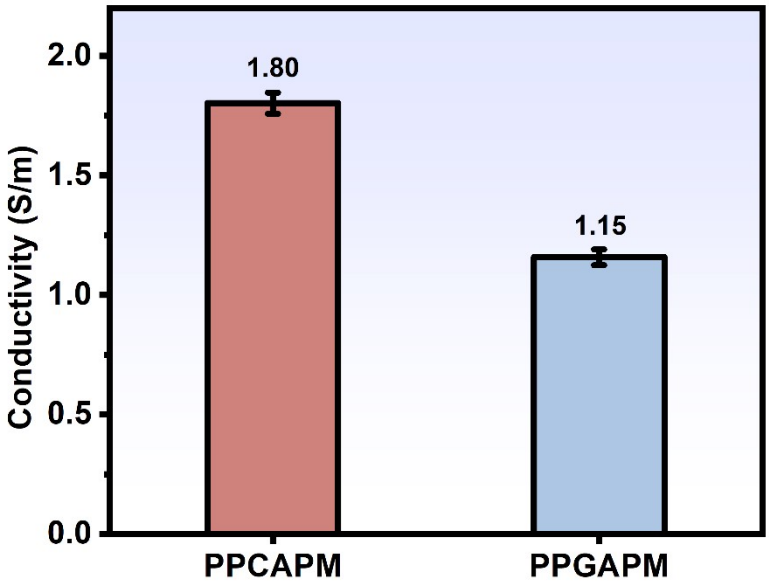

Fig. S10. The electrical conductivity of PPCAPM and PPGAPM composite hydrogels after 4 h at -40 ℃.

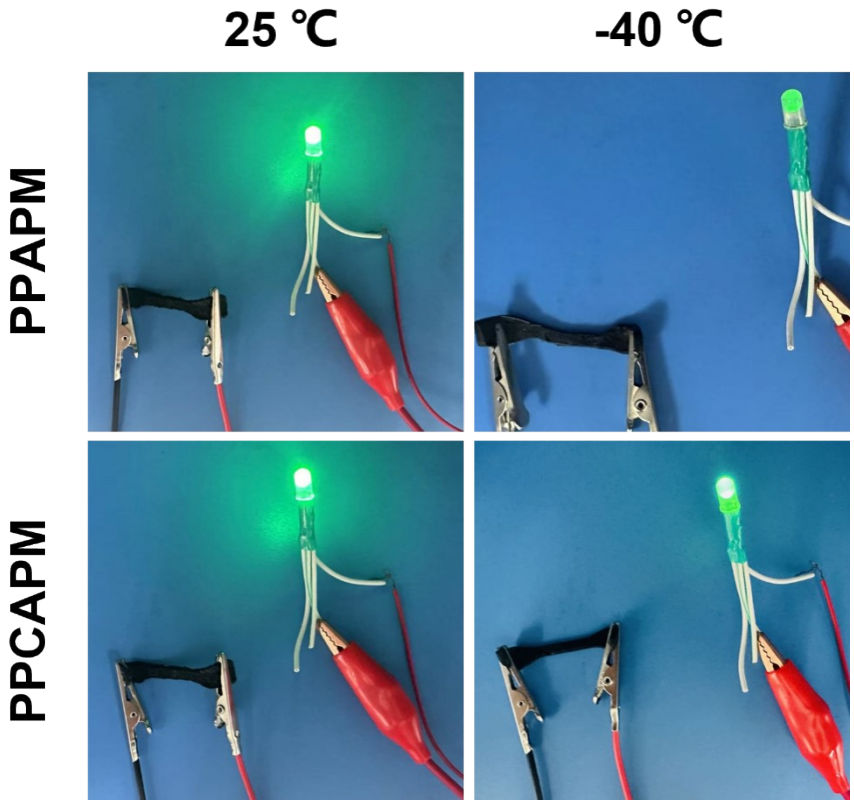

Fig. S11. Comparison of LED brightness in circuits using PPAPM and PPCAPM composite hydrogels as conductive wires at 25 ℃ and -40 ℃.

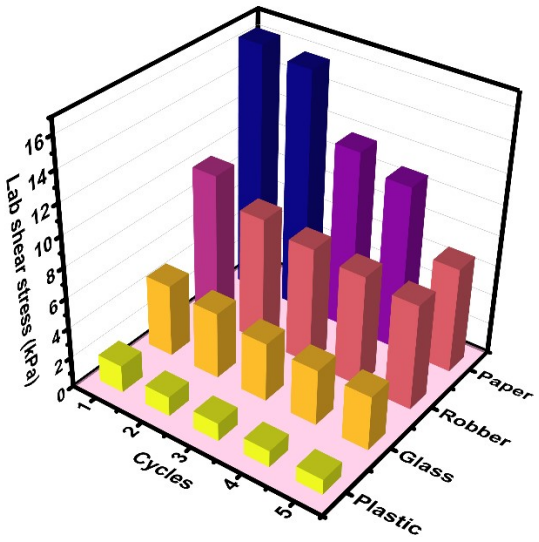

Fig. S12. The adhesion stability of PPCAPM composite hydrogel at -40 ℃ was observed.

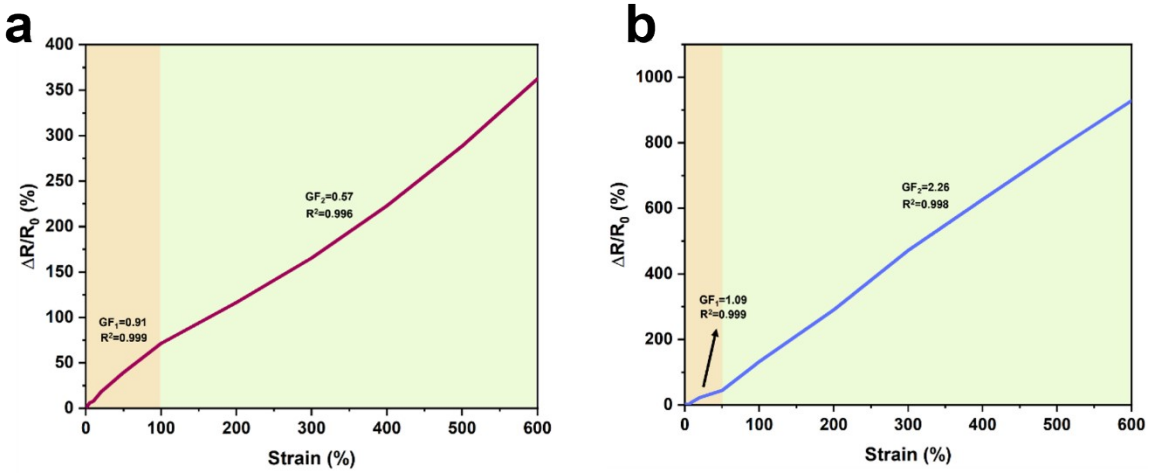

Fig. S13. The sensitivity of PPC and PPCM hydrogel.

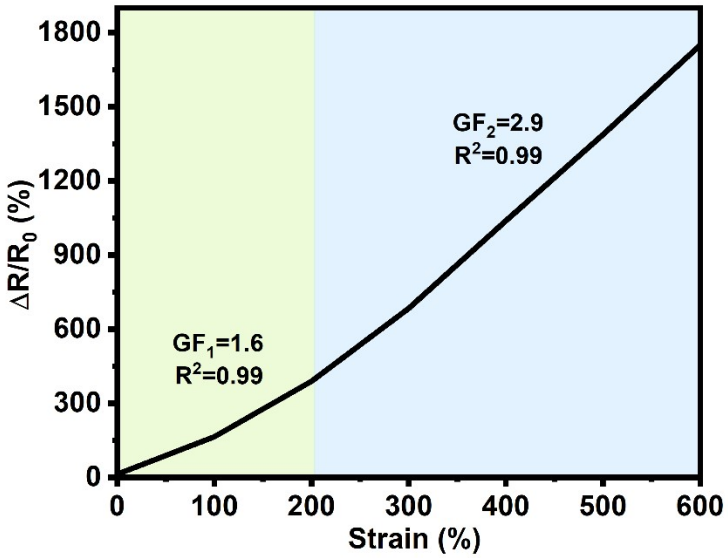

Fig. S14. Strain-dependent gauge factor of PPCAPM composite hydrogel at -40 ℃.

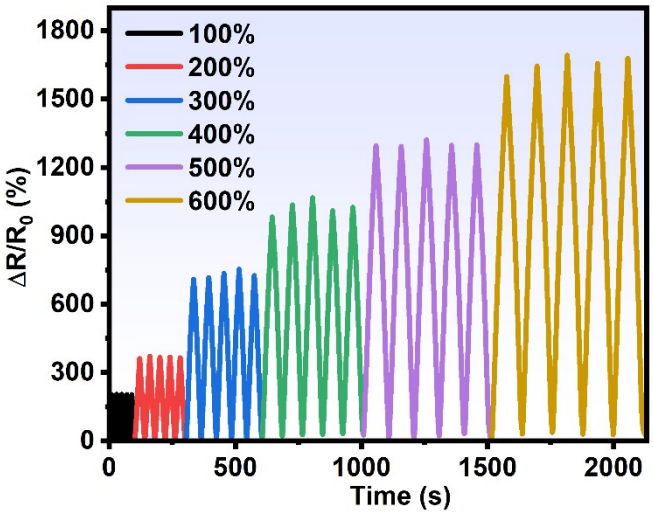

Fig. S15. Cyclic ($\Delta R/R_0$) response under varying strain amplitudes of PPCAPM composite hydrogel at -40 ℃.

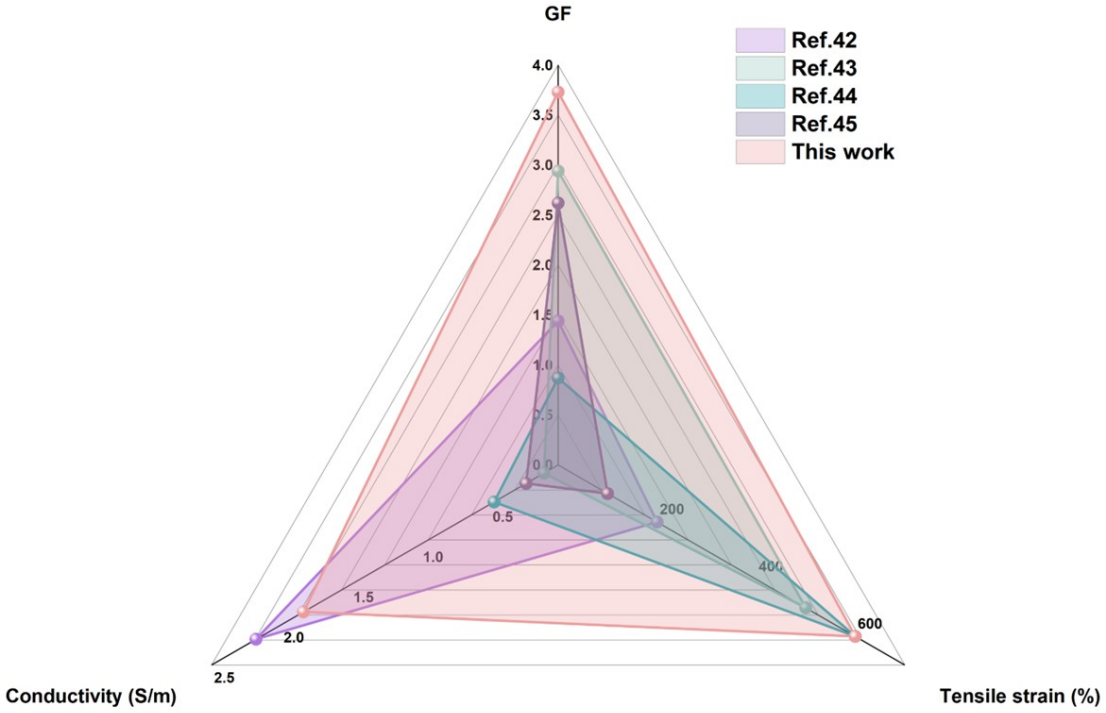

Fig. S16. Performance comparison between the PPCAPM composite hydrogel sensor and the currently reported hydrogel-based sensors in terms of sensitivity, maximum operating range, and electrical conductivity.

Table S1. Formulation of the prepared hydrogels.

	AM (g)	PVA (g)	TEMED (μL)	PA (mg)	$CaCl_2$ (g)	MXene (mg)	$AgNO_3$ (mmol)	H_2O (mL)
PP	1.4	0.8	25	0	0	0	0	10
PPC	1.4	0.8	25	0	3	0	0	10
PPM	1.4	0.8	25	0	0	50	0	10
PPCM	1.4	0.8	25	0	3	50	0	10
PPAPM	1.4	0.8	25	8	0	50	0.02	10
PPC_1APM	1.4	0.8	25	8	1	50	0.02	10
PPCAPM	1.4	0.8	25	8	3	50	0.02	10
PPC_5APM	1.4	0.8	25	8	5	50	0.02	10
PPGAPM	1.4	0.8	25	8	0	50	0.02	10